Multistability of Vector Solitons in High-Q Resonators

B. Kostet, Y. Soupart, E. Averlant, K. Panajotov, and M. Tlidi

Abstract We investigate the formation of vector solitons in weakly birefringent high-Q resonators. The presence of nonlinear polarization mode coupling in optical resonators subject to a coherent optical injection allows stabilizing up to two families of bright or dark vector dissipative solitons, depending on the dispersion properties of the system. We use coupled Lugiato–Lefever equations to investigate the dynamical properties of interacting laser fields confined in the Kerr optical resonators. Anomalous and normal dispersion regimes are considered, and it is shown that in both cases two branches of dissipative solitons coexist and exhibit different peak powers and different polarization properties. In these regimes, the input–output characteristics possess either a bistable or a tristable homogeneous response. The coexistence of two branches of localized states is not possible without taking into account the polarization degrees of freedom. The stabilization mechanism of these localized states is attributed to a subcritical modulational instability in the case of anomalous dispersion and to a front-locking mechanism in the normal dispersion regime. Their bifurcation diagrams exhibit either a homoclinic or a heteroclinic snaking type of instability, depending on the dispersion properties.

B. Kostet (✉) · Y. Soupart · E. Averlant · M. Tlidi
Département de Physique, Faculté des Sciences, Université Libre de Bruxelles (U.L.B.), CP 231, Campus Plaine, 1050 Bruxelles, Belgium
e-mail: Bilal.Kostet@ulb.be

Y. Soupart
e-mail: Youri.Soupart@ulb.be

E. Averlant
e-mail: e.averlant@ernestrichard.edu.brussels

M. Tlidi
e-mail: Mustapha.Tlidi@ulb.be

K. Panajotov
Department of Applied Physics and Photonics (IR-TONA), Vrije Universiteit Brussels, Pleinlaan 2, 1050 Brussels, Belgium
e-mail: kpanajot@b-phot.org

Institute of Solid State Physics, Bulgarian Academy of Sciences, 72 Tzarigradsko Chaussee Boulevard, 1784 Sofia, Bulgaria

L. Brenig et al. (eds.), *Nonequilibrium Thermodynamics and Fluctuation Kinetics*, Fundamental Theories of Physics 208,
https://doi.org/10.1007/978-3-031-04458-8_17

1 Introduction

Dissipative structures are inherent to out-of-equilibrium systems that are subject to mechanisms that tend to restore uniformity (a transport process such as diffusion, dispersion, diffraction, or thermal conductivity) and which compete with nonlinear interactions that tend to locally amplify the field intensity (chemical reactions or matter–light interaction), while dissipation of energy competes with injection [1, 2]. These properties can be found in many real-life systems, e.g. in the fields of chemistry [3, 4], biology [5], ecology [6–9], and nonlinear optics [10–12]. Dissipative structures can be spatially extended patterns and/or localized in time. In the first case, the organization of matter or energy in the bulk of the material often originates from a modulational instability (MI). Some of the most common spatial patterns are stripes, hexagons, and honeycombs [13]. Furthermore, when the modulational instability appears subcritically, there can exist a pinning region where isolated spots of the pattern are embedded on a homogeneous background which are often called dissipative solitons (DSs) [14]. Another type of dissipative solitons that can appear in the presence of bistability, without any pattern or any specific wavelength emerging, is due to the front-locking mechanism [15, 16]. In this case, the interaction of two fronts, i.e. heteroclinic connections between the two stable homogeneous steady states (HSSs), (also called continuous wave, CW solutions in optics), is responsible for the appearance of the DSs. For both of these formation mechanisms, the two balances between the nonlinear effect and the transport process on the one hand, and between pumping and dissipation on the other hand, make the DSs robust structures with an intrinsic size defined by the dynamical properties of the system only. This leads to very interesting prospects in the field of optics for possible applications such as information processing and optical storage [17–19].

Staying in the field of optics, considering the polarization degrees of freedom leads to richer dynamics. In free propagation, i.e. in the absence of an optical resonator, it has been shown that new modulational instabilities can appear, and with them, symmetry breaking, domain wall vector solitons, rotating vector soliton bound states [20], dark–bright vector solitons [21] and vector flat-top solitons [22]. In the presence of a Kerr resonator, the third-order dependency of the polarization on the electric field implies that the medium becomes birefringent. In particular, when the polarization state of the DSs evolves in time while the group velocities of the two different polarization components are locked, they are called group-velocity-locked vector solitons (GVLVSs) [23, 24]. Another common case corresponds to the locking of the polarization states of the two components, called polarization-locked vector solitons (PLVSs) [25, 26]. Other situations exist, such as vector solitons with locked and precessing states of polarization [27] or group-velocity-locked vector soliton molecules [28].

Most of the above-mentioned physical systems are spatially extended, where DSs correspond to spots in the two- or three-dimensional bulk of the material. However, in the field of nonlinear optics, they can be obtained in small area waveguides where diffraction can be neglected, so that the transport phenomenon role is carried out

by the chromatic dispersion of light. In this case, the DSs are called temporal DSs and present themselves as pulses propagating indefinitely in the cavity without any spreading of their temporal profile. This makes the temporal DSs very attractive for information processing as they could serve as bits in an all-optical buffer [29–31]. Another property of temporal DSs gathering ever more increasing interest is the optical spectrum built over many roundtrips in the cavity, which is made of equally spaced lines, also called optical frequency combs, allowing a myriad of applications in spectroscopy, metrology, and photonics [32–35]. When the generation of these optical frequency combs is due to the nonlinearity of a Kerr medium, they are called Kerr combs. In particular, a lot of this interest has been focused on high-Q resonators which have seen rapid development in recent years. This is partly due to their ability to host the Kerr combs in small devices with low pump power and various other important properties such as on-chip integration [36], octave-spanning spectra [37], or tuning of the central frequency [38].

In this chapter, we investigate numerically the formation of vector temporal solitons with different polarization states and intensities in optical resonators for different cases. This approach is valid for both all-fiber macroscopic resonators and microscopic resonators. First, we consider the anomalous dispersion regime in which we investigate bright DSs generated by the patterning phenomenon of modulational instability. We pursue with the normal dispersion regime where we place ourselves far from any MI, with low detunings and bistability between stable CW solutions, and consider dark DSs generated by the front-locking mechanism. In the case of higher detunings, we show that the polarization degrees of freedom lead to the appearance of tristability of stable CWs, bringing a high degree of multistability of DSs with very different polarization states.

2 The Vectorial Lugiato–Lefever Model

In 1987, L. A. Lugiato and R. Lefever theoretically evidenced the possibility of a spontaneous emergence of spatial stationary dissipative structures in the transverse plane of a laser beam circulating in a passive optical resonator filled with a nonlinear Kerr medium [10]. They provided a model allowing for the description of the spatio-temporal evolution of the electric field envelope E in such a system and that is since known as the Lugiato–Lefever equation (LLE) :

$$\frac{\partial E}{\partial t} = E_i - (1 + i\theta)E + i|E|^2 E + i\frac{\partial^2 E}{\partial x^2}. \tag{1}$$

Here, t is the normalized time, x is the normalized coordinate along the cavity, and θ is the frequency detuning of the injected field to the cavity resonance frequency. The self-organization of the electric field within this out-of-equilibrium system and the robustness of the resulting structures are explained by the appropriate balances of, on the one hand, diffraction with nonlinearity and, on the other hand, of the internal

losses with the pump E_i. This breakthrough in the field of nonlinear optics aroused a great interest among the scientific community, and the Lugiato–Lefever (LL) model was (and still is) widely used and developed.

Our purpose here is to adapt the LLE in order to take into account the polarization degrees of freedom of the electric field propagating inside a passive optical resonator. Moreover, when the transverse dimensions can be neglected (e.g. by using waveguides), so can the diffraction. The transport phenomenon playing its role is the chromatic dispersion and it is possible to find stable structures that are now localized in time instead of space. Such *temporal* dissipative solitons form a pulse train in the output branch of the resonator whose power spectral distribution is made out of evenly spaced teeth, forming so-called optical frequency combs. Adding a polarization degree of freedom will result in a vectorial LL model made out of two coupled LLEs, one for each polarization component of the electric field. Let us first briefly recall basic notions about polarization and how to characterize it. The reader familiar with the Stokes parameters and the polarization ellipse can skip the next section.

Characterizing the Polarization

In this section, we recall the fundamental notions and quantities necessary to study light polarization following the presentation made in [39]. From a classical point of view, the propagation of light corresponds to the spatio-temporal evolution of an electromagnetic wave constituted of an electric and a magnetic field oscillating perpendicularly relative to one another and both lying in the plane normal to the direction of propagation. Transverse waves such as electromagnetic waves possess a fundamental property called *polarization* describing the oscillatory behavior of the electric field vector in the transverse plane. Polarization of incoming light can be constantly evolving with time in a random fashion. Such light is said to be *unpolarized*. In that case, during the spatio-temporal evolution of the electric field, the successive orientations of the vector are uncorrelated and no dominant polarization state emerges. However, polarization is a central concept in nonlinear optics and laser physics since lasers generally produce quasi-monochromatic light which is always at least partially polarized. Different quantities can be used to characterize the polarization properties of an electric field $\mathbf{E}$ based on its components in the transverse plane (E_x, E_y). Among them, widespread are the *Stokes parameters*, defined as

$$\mathbf{S} = \begin{bmatrix} S_0 \\ S_1 \\ S_2 \\ S_3 \end{bmatrix} = \begin{bmatrix} |E_x|^2 + |E_y|^2 \\ |E_x|^2 - |E_y|^2 \\ E_x^* E_y + E_x E_y^* \\ i(E_x E_y^* - E_x^* E_y) \end{bmatrix} = \begin{bmatrix} P_h + P_v \\ P_h - P_v \\ P_{\pi/4} - P_{3\pi/4} \\ P_l - P_r \end{bmatrix} \in \mathbb{R}^4, \tag{2}$$

where * stands for the complex conjugate.

While S_0 is the total intensity, S_1 and S_2 give information about the fluxes of light polarized *linearly* along the horizontal x-direction (P_h) and the vertical y-direction (P_v) and along the directions at angles 45° ($P_{\pi/4}$) and 135° ($P_{3\pi/4}$) with respect to the x-direction, respectively. The sign of S_1 and S_2 indicates which flux overcomes

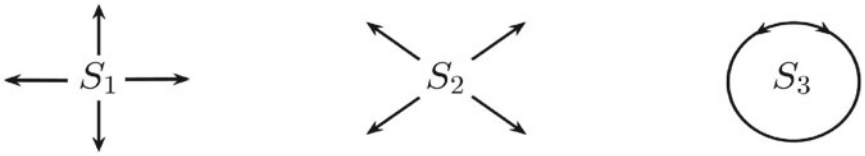

Fig. 1 Schematic representation of the Stokes parameters. The oscillations of the electric field in the transverse plane along the horizontal x-direction and the vertical y-direction are captured by S_1 while S_2 gives informations about the directions at angles $\pi/4$ and $3\pi/4$ with respect to the horizontal direction. Finally, S_3 quantifies the amount of right ($S_3 < 0$) or left ($S_3 > 0$) circularly polarized light

the other while their magnitude quantifies that excess. Finally, the *circular* polarization is described by parameter S_3, whose sign tells us if it is left-handed ($S_3 > 0$) or right-handed ($S_3 < 0$). Considering a light beam propagating in the z-direction (normal to the page), Fig. 1 gives a schematic representation of the Stokes parameters, sometimes seen as the components of a quantity $\mathbf{S}$, the Stokes (pseudo-)vector (as it does not transform as a vector), and fully describing the polarization state of light. Note that we generally work with the normalized quantities $s_i = S_i/S_0 \in [-1, 1]$.

Pure polarization states as presented in Fig. 1 are given by $\mathbf{s}_1 = [1, \pm 1, 0, 0]^T$, $\mathbf{s}_2 = [1, 0, \pm 1, 0]^T$, and $\mathbf{s}_3 = [1, 0, 0, \pm 1]^T$. However, in general, the tip of the electric field vector draws an ellipse in the course of its evolution, combining non-zero linear and circular components of polarization.

Based on the Stokes parameters and in order to complete our characterization of the polarization state of the output light, we can define several other quantities. The *degree of polarization* (DoP) takes a value between 0 and 1 and is the ratio of the total polarized flux and the total flux:

$$\mathrm{DoP}(\mathbf{S}) = \sqrt{s_1^2 + s_2^2 + s_3^2}. \tag{3}$$

Unpolarized light exhibits a zero DoP whereas light in a single state of polarization is fully polarized and the corresponding DoP is equal to 1. That general feature can be refined into its constitutive parts, namely the *degree of linear polarization* (DoLP) and the *degree of circular polarization* (DoCP), given by

$$\mathrm{DoLP}(\mathbf{S}) = \sqrt{s_1^2 + s_2^2}, \quad \text{and} \quad \mathrm{DoCP}(\mathbf{S}) = s_3. \tag{4}$$

DoLP varies from 0 (for circularly polarized or unpolarized light) to 1 (for linearly polarized light) while DoCP goes from -1 (for left circular polarization) to 1 (for right circular polarization). Light that is either unpolarized or linearly polarized has a DoCP of 0.

In the general case, we can define the ellipticity ϵ of the polarization ellipse

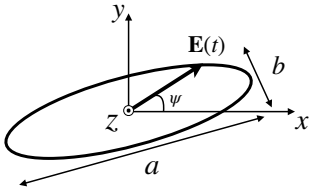

Fig. 2 Polarization ellipse in the (x, y)-transverse plane for light propagating in the z-direction. The major and minor axes of the ellipse are denoted by a and b, respectively

$$\epsilon = \frac{|s_3|}{\sqrt{s_1^2 + s_2^2 + s_3^2} + \sqrt{s_1^2 + s_2^2}} = \frac{b}{a}, \tag{5}$$

which is the ratio of the minor axis to the major axis of the ellipse describing the trajectory followed by the tip of the electric field vector (see Fig. 2).

Vectorial LL model

We consider the propagation of light inside a Kerr resonator submitted to coherent optical pumping (see Fig. 3). The ring cavity is filled with a birefringent medium, and its slow and fast axes are oriented along the x- and y-directions, respectively. This model is suitable to describe macroscopic fiber cavities as well as microscopic resonators. We take into account the polarization degrees of freedom and we neglect the phenomenon of diffraction so that the nonlinearity of the medium balances with the chromatic dispersion only, and the field only varies along the longitudinal direction. The Brillouin and Raman scatterings are not considered so that, over one roundtrip, the linear polarization components $\hat{E}_{x,y}(z, \tau)$ of the slowly varying electric field envelope obey the nonlinear Schrödinger equations that take the general forms [40]:

$$\frac{\partial \hat{E}_x}{\partial z} + \hat{\beta}_{1,x}\frac{\partial \hat{E}_x}{\partial \tau} + i\hat{\beta}_{2,x}\frac{\partial^2 \hat{E}_x}{\partial \tau^2} + \frac{\alpha_{i,x}}{2}\hat{E}_x = i\gamma\left(|\hat{E}_x|^2 + \frac{2|\hat{E}_y|^2}{3}\right)\hat{E}_x + \frac{i\gamma}{3}\hat{E}_x^*\hat{E}_y^2 e^{-2i\Delta\hat{\beta}z}, \tag{6a}$$

$$\frac{\partial \hat{E}_y}{\partial z} + \hat{\beta}_{1,y}\frac{\partial \hat{E}_y}{\partial \tau} + i\hat{\beta}_{2,y}\frac{\partial^2 \hat{E}_y}{\partial \tau^2} + \frac{\alpha_{i,y}}{2}\hat{E}_y = i\gamma\left(|\hat{E}_y|^2 + \frac{2|\hat{E}_x|^2}{3}\right)\hat{E}_y + \frac{i\gamma}{3}\hat{E}_y^*\hat{E}_x^2 e^{2i\Delta\hat{\beta}z}, \tag{6b}$$

where * stands for the complex conjugate. The spatial variable z represents the longitudinal coordinate while the temporal variable $\tau = t - \hat{\beta}_1 z$ is expressed in a reference frame moving at the mean group-velocity : $\hat{\beta}_1 = |\hat{\beta}_{1,x} + \hat{\beta}_{1,y}|/2 = v_g^{-1}$. Indeed, the first-order dispersion coefficient $\hat{\beta}_{1,j}$ represents the inverse speed of

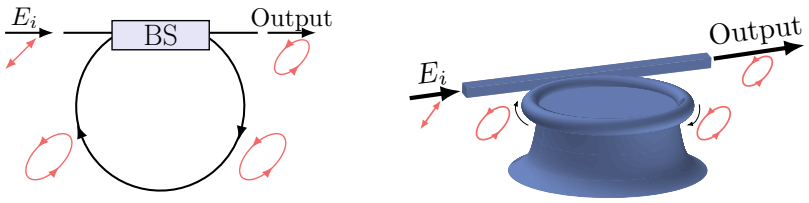

Fig. 3 (Left) Schematics of a typical optical macroscopic fiber resonator pumped with a linearly polarized field coherently coupled to the intracavity field at the beam splitter (BS). (Right) Schematics of a microscopic toroidal resonator or microring cavity. We will see in the next sections that the electric field adopts a elliptical polarization along its path in the cavity. Reproduced from [41]

the envelope of the electric field component $\hat{E}_j$ in the material. The second-order dispersion coefficient $\hat{\beta}_{2,j}$ characterizes the group-velocity dispersion of component $\hat{E}_j$ and we neglect higher order terms in the expansion of the propagation constant around the carrier frequency ω_0:

$$\hat{\beta}_j(\omega) = \sum_{k=0}^{\infty} \frac{\hat{\beta}_{k,j}}{k!}(\omega - \omega_0)^k, \quad \hat{\beta}_{k,j} = \left.\frac{d^k \hat{\beta}_j}{d\omega^k}\right|_{\omega_0}. \tag{7}$$

The zeroth-order coefficient $\Delta\hat{\beta} = \hat{\beta}_{0,x} - \hat{\beta}_{0,y} = 2\pi|n_x - n_y|/\lambda$ represents the difference between wavenumbers corresponding to the polarization components and therefore characterizes the birefringence of the material. The parameters $\alpha_{i,j}$ stands for the internal linear losses in each direction of polarization. Finally, the nonlinear coefficient γ accounts for the Kerr nonlinearity.

In order to consider the superposition of the intracavity field with the linearly polarized input beam, we impose the following boundary conditions coupling the fields at roundtrips m and $m + 1$:

$$\hat{E}^{m+1}_{x,y}(z = 0, \tau) = \sqrt{T}\,\hat{E}_{ix,iy} + \sqrt{R}e^{-i\delta_{x,y}}\hat{E}^{m}_{x,y}(L, \tau), \tag{8}$$

where T and R are, respectively, the intensity transmission and reflection coefficients at the beam splitter, $\hat{E}_{ix,iy}$ are the polarization components of the source field, and $\delta_{x,y}$ are the phase differences between the injected field and the circulating field after having traveled a cavity length L. To derive the mean-field Lugiato–Lefever model, we integrate the field equations (6) over one roundtrip and apply the boundary conditions (8). Under the assumptions of high-finesse ($T \ll 1$), and of detuning and coupling coefficient of order 1, we introduce the continuous limit by $t = mt_R$ and

$$\frac{\partial \hat{E}_{x,y}(t, \tau)}{\partial t} = \frac{\hat{E}^{m+1}_{x,y}(z = 0, \tau) - \hat{E}^{m}_{x,y}(z = 0, \tau)}{t_R}, \tag{9}$$

with t_R the cavity roundtrip time and t a slow time variable describing the field evolution from one roundtrip to another. We can now write the vectorial Lugiato–Lefever model as two coupled evolution equations for the polarization components of the renormalized electric field envelopes $E_{x,y}$ [42, 43],

$$\frac{\partial E_x}{\partial t} = E_i \cos(\psi) - (1 + i\theta_x)E_x + i\left(|E_x|^2 + \frac{2}{3}|E_y|^2\right)E_x + \Delta\beta_1 \frac{\partial E_x}{\partial \tau} + i\eta \frac{\partial^2 E_x}{\partial \tau^2}, \tag{10a}$$

$$\frac{\partial E_y}{\partial t} = E_i \sin(\psi) - (1 + i\theta_y)E_y + i\left(|E_y|^2 + \frac{2}{3}|E_x|^2\right)E_y - \Delta\beta_1 \frac{\partial E_y}{\partial \tau} + i\eta \frac{\partial^2 E_y}{\partial \tau^2}. \tag{10b}$$

It has to be noted that, in what follows, the fast time τ will be interpreted as a spatial variable. Indeed, knowing the group-velocity of light within the cavity of fixed length L, we can identify a position corresponding to each time τ . Consequently, for a given roundtrip (meaning that we fix the value of t), the observation of $E(t, \tau)$ over the interval going from $\tau = 0$ to $\tau = t_R = L\frac{n}{c}$ precisely gives the evolution of the electric field along the cavity for the selected round trip, as τ is expressed in a reference frame moving at the group-velocity of light in the cavity. The following renormalization factors were used in order to obtain the non-dimensional system of equations (10) :

$$E_{x,y} = \sqrt{\frac{\gamma L}{\alpha}}\hat{E}_{x,y}, \qquad E_{ix,iy} = \sqrt{\frac{\gamma L T}{\alpha^3}}\hat{E}_{ix,iy}, \tag{11}$$

$$t = \frac{\alpha}{t_R}t', \qquad \tau = \sqrt{\frac{2\alpha}{|\hat{\beta}_2|L}}\tau', \tag{12}$$

$$\theta_{x,y} = \frac{1}{\alpha}\delta_{x,y}, \qquad \beta_{1,x,y} = \sqrt{\frac{2\alpha L}{|\hat{\beta}_2|}}\hat{\beta}_{1,x,y}. \tag{13}$$

We consider that the input field E_i is linearly polarized in a direction oriented with an angle ψ with respect to the slow axis and that the total losses $\alpha = (\alpha_i L + T)/2$ are the same for each direction of polarization and renormalized to 1. The frequency detunings between the injected field components and the closest corresponding cavity resonance are given by $\theta_{x,y}$ and we placed ourselves in a reference frame moving at a speed being the mean group-velocity between the polarization components, hence $\Delta\beta_1 = (\beta_{1,x} - \beta_{1,y})/2$. The parameter $\Delta\beta_1$ is known as the group-velocity mismatch (GVM) parameter; however, in what follows, we will assume that no GVM affects the propagation of light inside the cavity which is a reasonable approximation for practical applications [44]. The group-velocity dispersion (GVD) coefficient is taken to be the same in both directions. In other words, it is here assumed that the second-order dispersion acts identically on both components of polarization of the electric field. Parameter $\eta = \pm 1$ stands for the sign of the GVD. Finally, the factor 2/3 is the cross-phase modulation (XPM) coefficient through which occurs the coupling between the field components. We complete our discussion of the model by giving some physical values of the parameters that one can encounter in physical applications [29] and [45]. While using silica fibers for optical transmission of information, it is suitable to use a carrier wave of wavelength in the vicinity of $\lambda = 1.5\,\mu$m. Indeed,

in this spectral region, internal losses due to absorption and scattering can go down to $\alpha_i \approx 0.2$ dB/km. In this conditions, a typical value for the group-velocity dispersion coefficient is $\hat{\beta}_2 \approx -20$ ps^2/km. The nonlinear coefficient γ characterizes the nonlinear response of the material to the presence of the electric field and is of the order of 2 (W km)$^{-1}$. A typical value for the refractive index for silica optical fibers is $n \approx 1.467$. When considering optical frequency combs, a fundamental property is the free spectral range (FSR), corresponding to the constant spacing between spectral lines. This FSR is equal to the repetition rate of the propagating pulse in the cavity, $\frac{1}{t_R}$.

Linear stability analysis

The homogeneous steady state solutions (HSSs) of system (10) satisfy the conditions $\partial E^s_{x,y}/\partial\tau = \partial E^s_{x,y}/\partial t = 0$ and therefore obey the equations

$$I_{ix,iy} = \left[1 + \left(\theta_{x,y} - I_{x,y} - \frac{2}{3} I_{y,x}\right)^2\right] I_{x,y}, \tag{14}$$

with $I_{ix,iy} = E^2_{ix,iy}$ and $I_{x,y} = |E^s_{x,y}|^2$. For fixed values of the control parameters that are the frequency detunings $\theta_{x,y}$ and the injected field intensities $E_{ix,iy}$, Eq. (14) possesses up to five physical solutions. A linear stability analysis of the HSSs brings insights concerning the dynamics of the system as a function of the control parameters and allows one to identify regimes that are interesting to investigate. In the case of zero GVM ($\Delta\beta_1 = 0$), we will perform it by adding a small perturbation to the HSSs ($E_{x,y} = E^s_{x,y} + E'_{x,y}$) and splitting the fields components into their real and imaginary parts. To the first order in the perturbations $E'_{x,y}$, system (10) rewrites

$$\begin{aligned}
\frac{\partial E'_{x,r}}{\partial t} &= -E'_{x,r} + \theta_x E'_{x,i} - 2\left[E^s_{x,r}E'_{x,r} + E^s_{x,i}E'_{x,i} + \frac{2}{3}\left(E^s_{y,r}E'_{y,r} + E^s_{y,i}E'_{y,i}\right)\right] E^s_{x,i} \\
&\quad - \left(|E^s_x|^2 + \frac{2|E^s_y|^2}{3}\right) E'_{x,i} - \beta_2 \frac{\partial^2 E'_{x,i}}{\partial\tau^2}, \qquad (15a) \\
\frac{\partial E'_{x,i}}{\partial t} &= -E'_{x,i} - \theta_x E'_{x,r} + 2\left[E^s_{x,r}E'_{x,r} + E^s_{x,i}E'_{x,i} + \frac{2}{3}\left(E^s_{y,r}E'_{y,r} + E^s_{y,i}E'_{y,i}\right)\right] E^s_{x,r} \\
&\quad + \left(|E^s_x|^2 + \frac{2|E^s_y|^2}{3}\right) E'_{x,r} + \beta_2 \frac{\partial^2 E'_{x,r}}{\partial\tau^2}, \qquad (15b) \\
\frac{\partial E'_{y,r}}{\partial t} &= -E'_{y,r} + \theta_y E'_{y,i} - 2\left[E^s_{y,r}E'_{y,r} + E^s_{y,i}E'_{y,i} + \frac{2}{3}\left(E^s_{x,r}E'_{x,r} + E^s_{x,i}E'_{x,i}\right)\right] E^s_{y,i} \\
&\quad - \left(|E^s_y|^2 + \frac{2|E^s_x|^2}{3}\right) E'_{y,i} - \beta_2 \frac{\partial^2 E'_{y,i}}{\partial\tau^2}, \qquad (15c)
\end{aligned}$$

$$\frac{\partial E'_{y,i}}{\partial t} = -E'_{y,i} - \theta_y E'_{y,r} + 2\left[E^s_{y,r}E'_{y,r} + E^s_{y,i}E'_{y,i} + \frac{2}{3}\left(E^s_{x,r}E'_{x,r} + E^s_{x,i}E'_{x,i}\right)\right]E^s_{y,r} + \left(|E^s_y|^2 + \frac{2|E^s_x|^2}{3}\right)E'_{y,r} + \beta_2\frac{\partial^2 E'_{y,r}}{\partial\tau^2}, \tag{15d}$$

where subscripts r and i denote real and imaginary part, respectively.
We now specify the shape of the perturbations $\mathbf{E'}$ that are taken under the form of normal modes of constant amplitude $\tilde{\mathbf{E}}$ and of frequency and wavenumber $\lambda, \omega \in \mathbb{C}$, respectively, $\mathbf{E'} = \tilde{\mathbf{E}}\exp(\lambda t + i\omega\tau)$, with

$$\mathbf{E'} = \begin{bmatrix} E'_{x,r} \\ E'_{x,i} \\ E'_{y,r} \\ E'_{y,i} \end{bmatrix}, \quad \text{and} \quad \tilde{\mathbf{E}} = \begin{bmatrix} \tilde{E}_{x,r} \\ \tilde{E}_{x,i} \\ \tilde{E}_{y,r} \\ \tilde{E}_{y,i} \end{bmatrix}. \tag{16}$$

In order to investigate the temporal stability of the homogeneous states with respect to such perturbations, we substitute $\mathbf{E'}$ in Eq. (15) and set the spatial derivatives to zero. This leads us to the following eigenvalue problem:

$$\mathbf{M_T}\tilde{\mathbf{E}} = \lambda\tilde{\mathbf{E}} \tag{17}$$

with

$$\mathbf{M_T} = \begin{bmatrix} -1 - 2E^s_{x,r}E^s_{x,i} & \mathcal{A}_1 & -\frac{4}{3}E^s_{y,r}E^s_{x,i} & -\frac{4}{3}E^s_{y,i}E^s_{x,i} \\ \mathcal{A}_2 & -1 + 2E^s_{x,r}E^s_{x,i} & \frac{4}{3}E^s_{y,r}E^s_{x,r} & \frac{4}{3}E^s_{y,i}E^s_{x,r} \\ -\frac{4}{3}E^s_{x,r}E^s_{y,i} & -\frac{4}{3}E^s_{x,i}E^s_{y,i} & -1 - 2E^s_{y,r}E^s_{y,i} & \mathcal{A}_3 \\ \frac{4}{3}E^s_{x,r}E^s_{y,r} & \frac{4}{3}E^s_{x,i}E^s_{y,r} & \mathcal{A}_4 & -1 + 2E^s_{y,r}E^s_{y,i} \end{bmatrix}, \tag{18}$$

the temporal evolution matrix of the perturbation, and

$$\mathcal{A}_1 = \theta_x - 2\left(E^s_{x,i}\right)^2 - \left(|E^s_x|^2 + \frac{2|E^s_y|^2}{3}\right),$$
$$\mathcal{A}_2 = -\theta_x + 2\left(E^s_{x,r}\right)^2 + \left(|E^s_x|^2 + \frac{2|E^s_y|^2}{3}\right),$$
$$\mathcal{A}_3 = \theta_y - 2\left(E^s_{y,i}\right)^2 - \left(|E^s_y|^2 + \frac{2|E^s_x|^2}{3}\right),$$
$$\mathcal{A}_4 = -\theta_y + 2\left(E^s_{y,r}\right)^2 + \left(|E^s_y|^2 + \frac{2|E^s_x|^2}{3}\right).$$

For each value of the injection amplitude E_i, there are either one, three, or five physical homogeneous steady state solutions to the system (17) for each of which

correspond four eigenvalues of $\mathbf{M_T}$ that characterize the temporal evolution of the perturbation. More precisely, the real part λ_r of the temporal eigenvalue informs about the growth rate of the perturbation. If all λ_r are negative, the perturbation will die out and the system will fall back on the base state $\mathbf{E}^s$, which is subsequently qualified as *stable*. If, on the contrary, the dominant eigenvalue has a positive real part, $\mathbf{E}'$ will grow with time, driving the perturbed state $\mathbf{E}$ away from the base state $\mathbf{E}^s$. In that case, the base state is said to be *unstable* with respect to perturbations of the form $\mathbf{E}'$. A zero dominant eigenvalue prevents us to conclude from the restricted *linear* stability analysis. The imaginary part λ_i of the temporal eigenvalue characterizes modulations and periodic behavior in the temporal evolution of the perturbation.

Considering the stable stationary states, it is worth looking at the spatial evolution of the perturbation or, in other words, their spatial stability. Back to system (15), we now set the temporal derivative to zero, inject the perturbation (16), and isolate the spatially dependent terms. This results in the eigenvalue problem

$$\mathbf{M_S}\tilde{\mathbf{E}} = \Omega\tilde{\mathbf{E}} \tag{19}$$

with $\Omega = \omega^2$,

$$\mathbf{M_S} = -\frac{1}{\beta_2}\begin{bmatrix} \mathcal{B}_1 & 1-2E^s_{x,r}E^s_{x,i} & -\frac{4}{3}E^s_{x,r}E^s_{y,r} & -\frac{4}{3}E^s_{x,r}E^s_{y,i} \\ -1-2E^s_{x,r}E^s_{x,i} & \mathcal{B}_2 & -\frac{4}{3}E^s_{y,r}E^s_{x,i} & -\frac{4}{3}E^s_{y,i}E^s_{x,i} \\ -\frac{4}{3}E^s_{x,r}E^s_{y,r} & -\frac{4}{3}E^s_{x,i}E^s_{y,r} & \mathcal{B}_3 & 1-2E^s_{y,i}E^s_{y,r} \\ -\frac{4}{3}E^s_{x,r}E^s_{y,i} & -\frac{4}{3}E^s_{x,i}E^s_{y,i} & -1-2E^s_{y,r}E^s_{y,i} & \mathcal{B}_4 \end{bmatrix}, \tag{20}$$

the spatial evolution matrix of the perturbation, and

$$\begin{aligned}
\mathcal{B}_1 &= \theta_x - 2(E^s_{x,r})^2 - \left(|E^s_x|^2 + \frac{2|E^s_y|^2}{3}\right), \\
\mathcal{B}_2 &= \theta_x - 2(E^s_{x,i})^2 - \left(|E^s_x|^2 + \frac{2|E^s_y|^2}{3}\right), \\
\mathcal{B}_3 &= \theta_y - 2(E^s_{y,r})^2 - \left(|E^s_y|^2 + \frac{2|E^s_x|^2}{3}\right), \\
\mathcal{B}_4 &= \theta_y - 2(E^s_{y,i})^2 - \left(|E^s_y|^2 + \frac{2|E^s_x|^2}{3}\right).
\end{aligned}$$

Regarding the spatial stability, we focus on the presence of a *modulational instability* which is characterized by a transition in the spectrum of Ω from a pair of complex conjugated eigenvalues to real eigenvalues:

$$\Omega^{\text{init}} = \{a_1 \pm ia_2; b_1 \pm ib_2\} \rightarrow \Omega^{\text{fin}} = \{a_3; a_4; b_3 \pm ib_4\}, \tag{21}$$

with $a_1, a_2, a_3, a_4, b_1, b_2, b_3, b_4 \in \mathbb{R}_*^+$.
Indeed, for stationary states, if the dynamics of the perturbation (16) is characterized by a real wavenumber $\omega \in \mathbb{R}$, then it evolves as $\mathbf{E}' = \tilde{\mathbf{E}} \exp(\tilde{\omega}\tau)$ where $\tilde{\omega} = i\omega$ is purely imaginary. Consequently, the perturbation leads to a modulation of the amplitude of the electric field along the cavity, without global growth or decay, and results in the formation of a periodic pattern (sometimes called wavetrain) filling the cavity. In the fields of nonlinear optics and laser physics, the transition (21) is referred to as modulational instability.

3 Modulational Instability in the Case of Anomalous Dispersion

In this section, we investigate how the polarization of light affects the usual solutions found in the LL model in the case where the second-order dispersion is anomalous, i.e. $\eta = +1$. We begin with a standard linear stability analysis of the continuous wave solutions in this case, with respect to a perturbation of the form $\exp(i\omega\tau + \lambda t)$. We fix the detuning along the fast axis θ_y, while θ_x and E_i are the control parameters. The resulting stability map in the parameter space is shown in Fig. 4. For some representative values of θ_x (cuts (a),(b), and (c)), the total intracavity field intensity $S_0 = |E_x|^2 + |E_y|^2$ is plotted as a function of the fast time τ in Fig. 5. Along these cuts, curves with positive slope ($\partial S_0/\partial E_i > 0$) are stable, while curves with negative slope ($\partial S_0/\partial E_i < 0$) are unstable. For very low values of θ_x, moving along the cut (a), (corresponding to the input–output characteristic curve Fig. 5a), we encounter the threshold from which the single stable CW state (region I) becomes a single modulationally unstable state (region II). For higher injection values, we enter the hysteresis loop (region IV) meaning that a domain of bistability between two modulationally unstable states appears. We can continue past the hysteresis loop, where only the upper modulationally unstable state is left.
As the detuning θ_x is increased (going upwards on the map), we can see that the value of the E_i threshold of the bistability between MI states (the border between regions II and IV) monotonically decreases, while the threshold of the MI bifurcation (the border between regions I and II) decreases before increasing again, at which point it becomes superseded by the birth of a new bistability, between one stable CW state and one modulationally unstable state (region III). Two distinct bistabilities exist for different ranges of the injection power at this point, as shown in the input–output characteristics Fig. 5b. The threshold corresponding to the disappearance of region III and the one corresponding to the appearance of region IV start converging for higher values of θ_x, until both different types of bistabilities coincide which leads to the red region V where one CW state coexists with two different modulationally unstable states. The cut (c) illustrates this region, with the corresponding CW intensity curve shown in Fig. 5c.

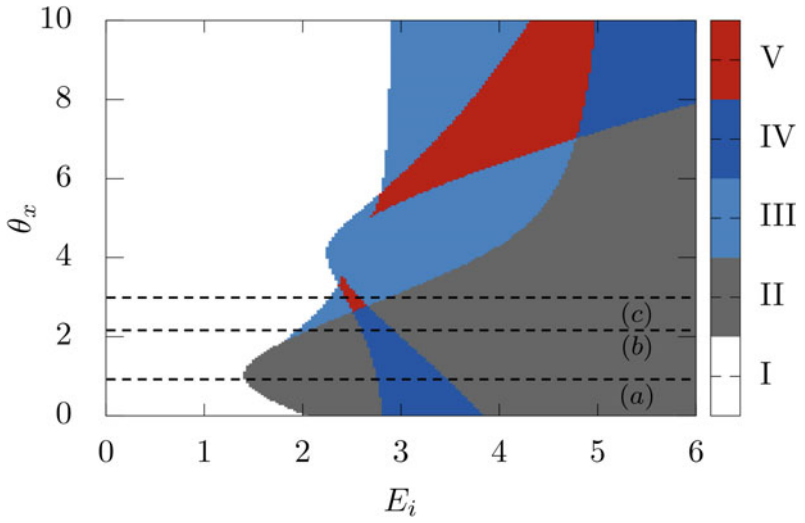

Fig. 4 Stability map of the CW solutions in the parameter plane (E_i, θ_x). Region I corresponds to parameters for which the system only hosts one single stable steady state. Region II corresponds to parameters for which the system only hosts one single modulationally unstable state. Region III corresponds to parameters for which the system hosts bistability between one stable steady state and one modulationally unstable state. Region IV corresponds to parameters for which the system hosts bistability between two modulationally unstable states. Region V corresponds to parameters for which the system hosts tristability between one stable steady state and two modulationally unstable states

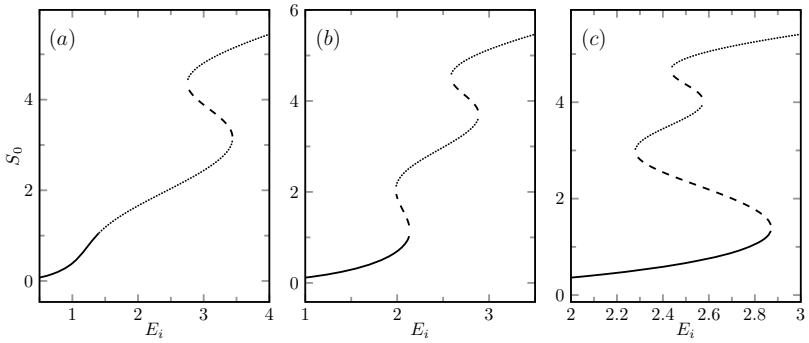

Fig. 5 Steady states corresponding to the cuts taken along the dashed lines in Fig. 4, with the total intensity S_0 given as a function of the injection for fixed values of the x detuning (**a**) $\theta_x = 1$, (**b**) $\theta_x = 2.25$, and (**c**) $\theta_x = 3$. Other parameters are the same as in Fig. 4. Full lines correspond to stable states, dashed lines correspond to unstable states, and dotted lines correspond to modulationally unstable states

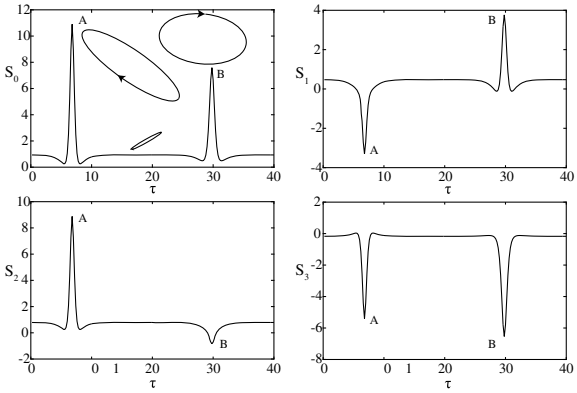

Fig. 6 Profiles of the non-normalized Stokes parameters S_0, S_1, S_2, and S_3 as a function of the fast time τ for two coexisting bright DSs with different properties. Parameters are $E_i = 2.54$, $\theta_x = 2.75$, *and* $\theta_y = 4.3$. Reproduced from [46]

The bistability between a stable CW state and a subcritically arising MI pattern is a key ingredient to the generation of DSs [11]. This coexistence leads to a range of the control parameter (where DSs can be stabilized) called the pinning range. Thanks to the polarization properties of our system, two different MI patterns exist, and in particular two different MI patterns can coexist with a stable CW state in the red areas of Fig. 4, meaning that it should be possible to generate two different types of DSs in this cavity for overlapping values of the two pinning ranges associated with each type of DS. This is shown in Fig. 6 with the profiles of two different bright DSs as a function of the fast time τ, obtained by direct numerical simulation of Eq. (10) with periodic boundary conditions. We show their total intensity S_0, and we characterize their polarization properties through the other non-normalized Stokes parameters S_1, S_2, and S_3, as defined in Sect. 2. S_0 is the total intensity of light. S_1 is the component of light that is linearly polarized along the axes x and y. S_2 also corresponds to light polarized linearly, but diagonally at 45° with respect to the x- and y-axes. S_3 is the circular component of the light polarization. The two DSs obtained in the same physical system clearly exhibit different intensities, with the brighter pulse on the left of the profile, since it has a higher peak power on the S_0 profile. The brighter DS is labeled A, while the darker one is labeled B. Their polarization properties are also quite different. The A-type DS has a negative S_1, representing a component of the polarization aligned with the y-axis. Its positive S_2 represents a component aligned at 45° with the x-axis, and finally, the negative S_3 indicates a right-handed circular component. The B-type DS has a positive S_1 (component aligned with the x-axis), negative S_2 (component aligned at 45°C with the x-axis), and negative S_3 (right-handed circular component). The background exhibits a very small positive S_2, a moderate positive S_3, and a very small negative S_3, so that its polarization is mostly aligned at 45° with the x-axis, showing only a very slight ellipticity.

It is well known that DSs generated by subcritical modulational instabilities exhibit bifurcation diagrams in the form of homoclinic snaking, emerging from the modulational instability bifurcation in the input–output characteristic curve [47]. We

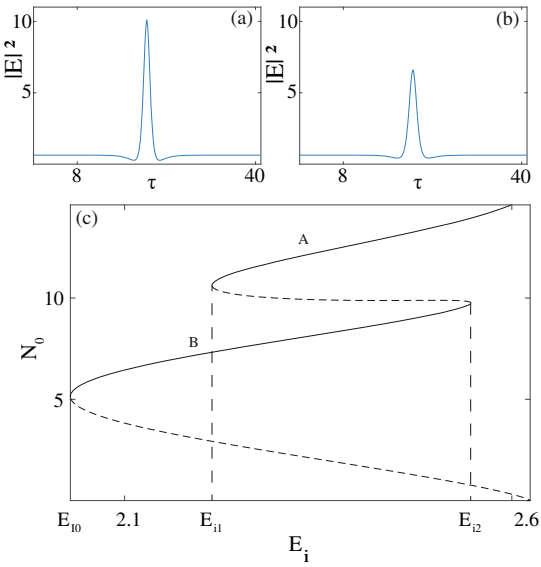

Fig. 7 (a) Profile of an A-type DS and (b) Profile of a B-type DS for fixed parameters of $E_i = 2.54$, $\theta_x = 2.75$, and $\theta_y = 4.3$. (c) Bifurcation diagram showing the L2-norm N_0 as a function of injected field amplitude E_i. Dashed (full) lines are unstable (stable) solutions. Reproduced from [46]

verify how this behavior changes due to the polarization by performing a numerical continuation in the parameter space with a predictor–corrector method initiated by a numerical simulation profile, both using periodic boundary conditions. The detuning parameters are all fixed, while the amplitude of the injection is varied. The results are shown in Fig. 7(c), where the normalized L2-norm $N_0 = \int (S_0 - \tilde{S}_0)/L \, \mathrm{d}\tau$ is shown as a function of E_i. $\tilde{S}_0$ corresponds to the CW intensity, so that the contribution of the background is removed from the norm. As usual for a homoclinic snaking, an unstable branch emerges from the MI bifurcation of the HSS, then reaches a turning point where it becomes stable, which corresponds to the B-type DS. The DS then grows for increasing injection amplitude, until it reaches a saddle-node bifurcation where the solution becomes unstable. Then, the unstable branch goes through another turning point where it becomes the stable A-type DS. There is only a finite range of parameters where the two types of DSs coexist, between the values E_{i1} and E_{i2}. The profiles of the two coexisting solitons, types A and B, are shown in Fig. 7a, b, respectively, for fixed parameters of $E_i = 2.54$, $\theta_x = 2.75$, and $\theta_y = 4.3$. Homoclinic snaking bifurcation diagrams usually present themselves in the form of two branches oscillating across the pinning range, one corresponding to an even number of identical peaks, and the other one corresponding to an odd number of identical peaks. These two branches continue until the DSs entirely fill up the cavity, and they connect back to the patterned state. The system is then highly multistable, as these solutions all coexist in the pinning range. In our case, the behavior is more complex, as the system can host different types of vector DSs. The numerical simulations shown in Fig. 8 illustrate what happens in this case. As usual, even or odd numbers of DSs hosted in the intracavity field each correspond to a homoclinic snaking branch. For the regions where both pinning ranges coexist, the main branches divide into

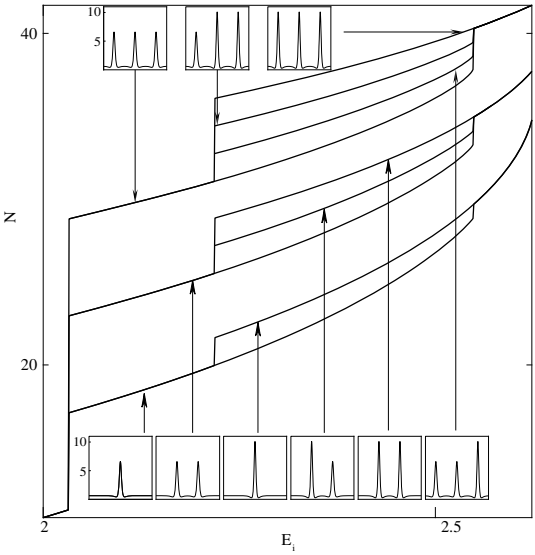

Fig. 8 Evolution of the L2-norm $\mathcal{N}$ as a function of injected field amplitude E_i for numerical simulations taken with a step of 0.001 for E_i. Reproduced from [46]

sub-branches for the different combinations of A-type and B-type DSs (see insets). In this figure, numerical simulations allow to draw the stable branches only.

4 Front-Locking in the Case of Normal Dispersion

In this section, we will be operating in the normal dispersion regime, i.e. $\eta = -1$, as this will allow us to avoid MI and focus on CW solutions only. Fronts, sometimes also called switching waves, are heteroclinic connections between different CWs. Their dynamics, including the generation of dark DSs, has been studied in the scalar case [48], without taking into account the polarization of light.

We start with the linear stability analysis of the CWs. Figure 9(a) shows the parameter space (θ_x, E_i), with a region of bistability between two stable CW states in blue, while white regions correspond to monostability. Figure 9(b) shows the bistable curve corresponding to a section of the map for a fixed value of θ_x. The system can host a mixed state, called front, connecting these two stable CWs as shown in Fig. 9(c). These fronts are generally not stationary. Depending on the value of the pump, one of the states will invade the other. For low values of E_i, the front will move toward regions where S_0 is higher, meaning that the CW corresponding to the lowest total intensity will invade the system (left panel). For high values of E_i, the front moves in the opposite direction and the CW corresponding to the highest total intensity will invade the system (right panel). There exists a point in-between, called the Maxwell point, where the front is stationary as both states are equally stable so that they will not invade each other.

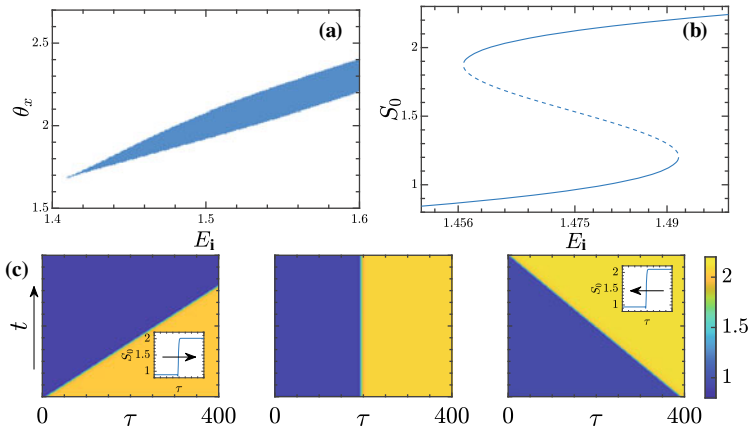

Fig. 9 (a) Stability map in the θ_x-E_i plane, with $\theta_y = 1.95$. The white (blue) region indicates monostability (bistability). (b) Bistable curve obtained for $\theta_x = 1.90$ and $\theta_y = 1.95$. Stable (unstable) CW states are denoted by solid (dashed) lines. (c) Front propagation to the right, below the Maxwell point (left panel: $E_i = 1.462$), at the Maxwell point (middle panel: $E_i = 1.46652$), and above the Maxwell point (right panel: $E_i = 1.471$). The boundary conditions are fixed to the CW values. Reproduced from [49]

We can notice that the fronts possess oscillatory tails on the bottom of their lower branch. This is an essential ingredient for the formation of DSs, as it is through these tails that the interaction between fronts is mediated. When the oscillations are absent, and the front is only exponentially decaying, there is no interaction between fronts so that it is impossible to stabilize the DSs [50–52]. The oscillatory tails however allow for an oscillatory potential of interaction with positive and repulsive interactions, depending on the relative positions of the fronts, and with equilibrium positions where those attractive and repulsive interactions are perfectly balanced. A numerical simulation with periodic boundary conditions of two fronts converging toward each other is summarized in the space–time map at the top of Fig. 10. In this case, the amplitude of the injected light is higher than the Maxwell point, so that the upper state tries to invade the system. The two well-separated fronts (Fig. 10(a)) then reach an equilibrium position as shown in Fig. 10(b), meaning that the repulsion of the fronts counterbalances their attraction as well as the front motion, and the DS is formed. In the case where the amplitude of the injected light is lower than the Maxwell point, the two fronts should start close enough so that the repulsive interaction will beat the invading motion and move them toward their equilibrium position. In our case, only the lower part of the fronts exhibit such oscillatory tails, so that only dark DSs will be formed. Two different dark DSs can be formed depending on the exact initial conditions, Fig. 10(b) or Fig. 10(c). The latter is the simplest solution, with a simple soliton consisting of only a dip in the total light intensity, while the first one is another more complex solution, with a single bump at the bottom of the profile. These two solutions thus can coexist for the same values of the parameters. They also

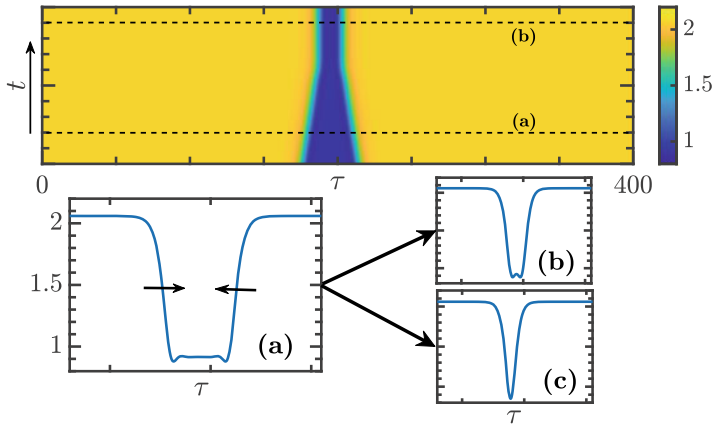

Fig. 10 Two fronts interact in an attractive way, which leads to the formation of vectorial dark dissipative solitons with the total intensity in the τ-t map (top panel). (**a**, **b**) Cross-sections along the dashed lines indicated in the τ-t map. **(c)** stable single dip DVDS. Numerical simulations of Eq. 10 are obtained for the parameters $E_i = 1.4675$, $\theta_x = 1.90$, and $\theta_y = 1.95$. Reproduced from [49]

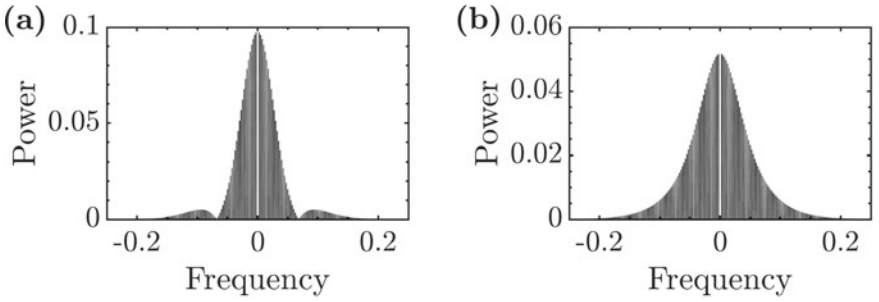

Fig. 11 Optical frequency combs corresponding to the two coexisting profiles shown in Fig. 10. Parameters are $E_i = 1.46655$, $\theta_x = 1.90$, and $\theta_y = 1.95$. Reproduced from [49]

have similar spectral properties, as the spectral contents of DSs are optical frequency combs shown in Fig. 11. The simplest DS shows an envelope in the shape of a sech^2 curve [34], while the solution from Fig. 10b shows additional bumps at each side of the envelope of the comb. The two combs share the same FSR, as this is only determined by the repetition rate which is the same for all of our DSs, since they move in the cavity with the same group velocity.

To investigate this coexistence, we show the bifurcation diagram for these two solutions with the detuning parameters fixed, the injected field amplitude as the control parameter, and we describe the branches through the normalized L2-norm $\mathcal{N} = \int S_0/L \mathrm{d}\tau$, where L is the size of the system. The profiles obtained through

numerical simulations were used to initiate a predictor–corrector continuation algorithm [53]. The so obtained diagram, shown in Fig. 12, is called a collapsed heteroclinic snaking, because the branch oscillates with an exponentially decreasing amplitude around the Maxwell point until it collapses on it. A closeup of the collapsed snaking curve is shown alongside the bifurcation diagram. Profiles associated with the points (a–h) are shown underneath the bifurcation diagram. Each turning point of the snaking curve corresponds to a change of stability, and a new stable state brings a new solution, with an additional bump at the extremum of the DS each time, as can be seen on profiles (a–d). This branch emerges from the point SN_1 where the CW regains its stability and the higher stable CW appears, and after oscillating and collapsing, it connects to the point SN_2 where the lower stable CW loses its stability. This point actually corresponds to a bifurcation to a MI state, that exists for a range of the injection amplitude that is extremely small before turning unstable. When the branch has collapsed on the Maxwell point and thus stops oscillating, the solution stops changing and only the width of the DS varies as we continue along the curve. Indeed, profiles (e–h) show that the width increases as we go down the branch, meaning that the lower state invades the entire system. At the end of this branch, we connect back to the lower stable CW at the point SN_2 as the lower state has entirely invaded the system.

The DSs formed by this mechanism are robust structures, and they can coexist in the same system as shown in Fig. 13 which depicts the space–time map of a numerical simulation with periodic boundary conditions, initialized with random noise added to a constant value between the two stable CWs. We also show their normalized Stokes parameters, S_0 to s_3, to illustrate that the two different coexisting dark DSs exhibit slightly different peak powers and polarization properties.

5 Tristability in the Case of Normal Dispersion

We will now consider the propagation of light in a pumped Kerr cavity in the normal dispersion regime for higher values of the detuning parameters. As this parameter is increased, the hysteresis loop formed by the CWs widens and undergoes new bifurcations. In particular, a second hysteresis loop can appear leading to the existence of three different solutions for the same value of the detuning, as shown by the linear stability analysis represented in Fig. 14 in the phase space (E_i, θ_x). In this map, light blue regions correspond to two stable solutions coexisting, while light red regions correspond to three stable solutions coexisting. At the very bottom of the figure (low values of θ_x), for a fixed value of the detunings and varying E_i, only one light blue region (II) is encountered, corresponding to a simple hysteresis loop. Higher in the map, two distinct blue regions can be encountered while varying E_i for fixed θ_x as highlighted by the dashed line (a), which is the above-mentioned case of two hysteresis loops. The input–output characteristics of the CWs for this cut are shown in Fig. 15(a) with the output intensity as a function of the injected field amplitude. Because the two hysteresis loops widen as the detuning is increased,

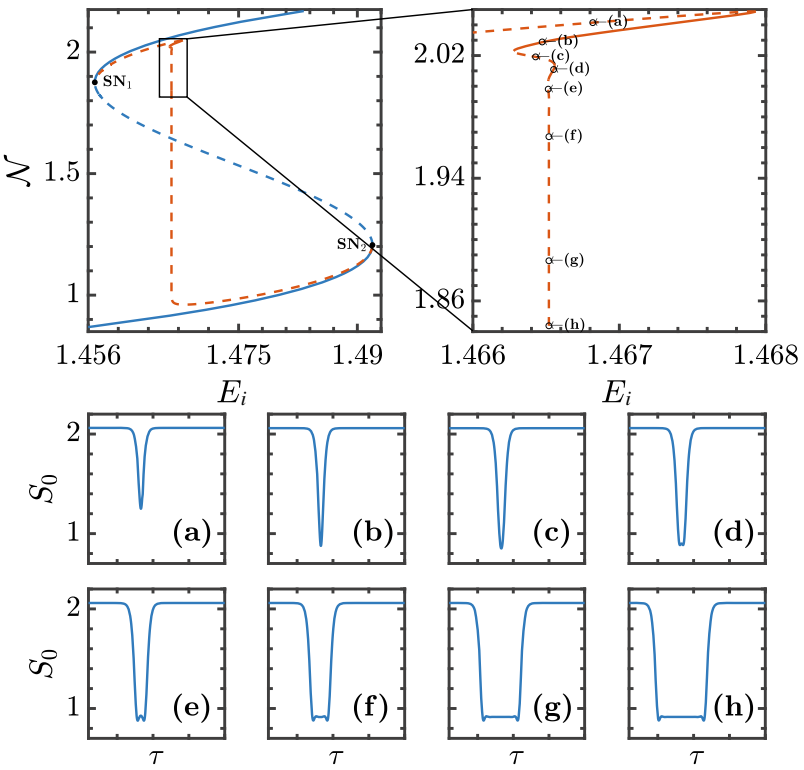

Fig. 12 Bifurcation diagram showing the L2-norm $\mathcal{N}$ as a function of injected field amplitude E_i. The right panel is a zoom around the snaking curve. Solid (dotted) curves correspond to stable (unstable) localized solutions. (**a**–**h**) Profiles of the total field intensity S_0. Parameters are $\theta_x = 1.90$ and $\theta_y = 1.95$. Periodic boundary conditions were used. Reproduced from [49]

they end up overlapping, leading to the first light red tristable region (IV). As θ_x is increased, this tristable region disappears as the upper hysteresis loop collapses into a single monotonous curve, going back into simple bistability represented by the light blue region II. The light red region IV then reappears for higher θ_x values through the inverse process, as a new hysteresis loop reappears near the upper saddle-node bifurcation. An example of tristable region is highlighted by the dashed line (b), for which the corresponding input–output characteristics of the CWs are shown in Fig. 15(b). This curve shows the coexistence of three stable solutions for the same value of all parameters. We can also notice in Fig. 14 the presence of regions with modulationally unstable states bordering on the right the bistable and tristable regions. These states will not be relevant here as we will operate far from them, and thus far from any branch corresponding to modulationally unstable states.

The polarization properties of each of these CW solutions are already of interest. Despite an injected light with a constant and completely linear polarization, cross-

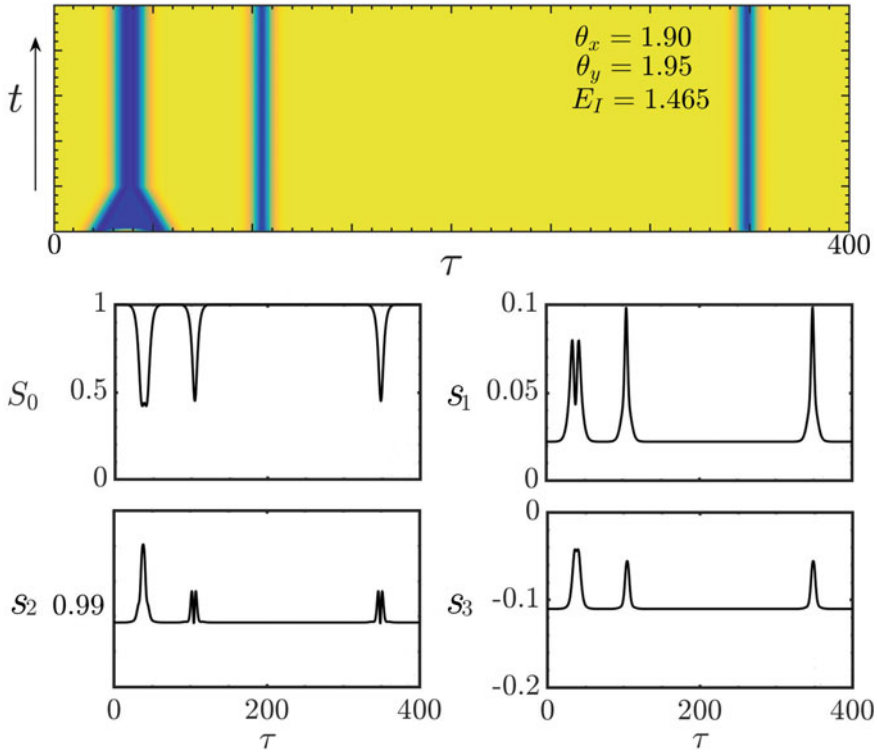

Fig. 13 (Top) (τ, t) map of the total intensity S_0. Parameters are the same as in Fig. 11. (Bottom) The Normalized Stokes parameters S_0, s_1, s_2, and s_3 as functions of the fast time τ. Reproduced from [49]

phase modulation (XPM) allows the intracavity fields to show a rich complexity in how each of the Stokes parameters evolves as shown in the previous sections. To investigate this further, the normalized Stokes parameters for the current set of parameters are shown in Fig. 16. All of the Stokes components undergo hysteresis loops at the same values of the pump, as those hystereses correspond to the ones from Fig. 15, but with very different output values, so that the three CWs exhibit very different polarization properties. The linear components can be in any configuration; however, one common trait between those CWs is that they are elliptically polarized, even if slightly. It can also be noted that the sign of s_3 changes between both curves Fig. 15(a) and Fig. 15(b), indicating that a change in the value of the detunings can also lead to notable variations in the polarization properties of the intracavity light.

Similarly to the previous section, the coexistence of stable CW solutions for fixed values of the parameters allows for fronts connecting them to emerge. The most important feature of these fronts is the presence of oscillatory tails damped around the CW, allowing two fronts evolving toward each other to interlock and subsequently constitute a stable structure embedded in a CW background and with a

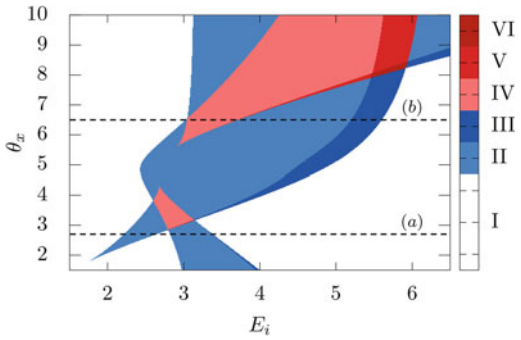

Fig. 14 Stability regions in the parameter space E_i–θ_x. Parameters are: $\theta_y = 5$ and $\eta = -1$. Region I corresponds to monostability, with the presence of only one stable state. Region II corresponds to bistability between two stable states. Region III corresponds to bistability between one stable state and one modulationally unstable state. Region IV corresponds to tristability between three stable states. Region V corresponds to tristability between two stable states and one modulationally unstable state. Finally, region VI corresponds to tristability between one stable state and two modulationally unstable states. Examples of two consecutive bistable curves and of a tristable curve along the dashed lines (**a**) and (**b**) are shown in Fig. 15a, b, respectively. Reproduced from [41]

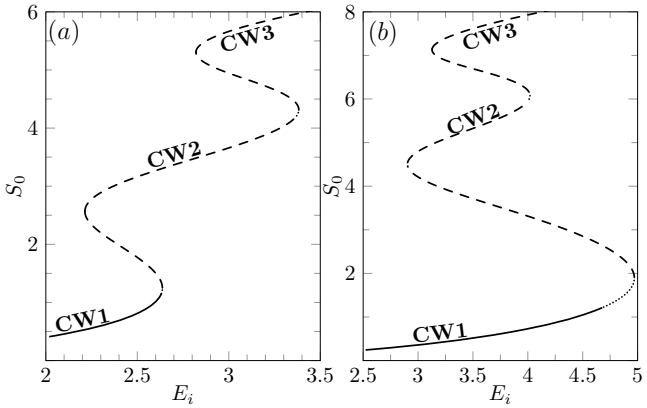

Fig. 15 Bistable curve (**a**) and tristable curve (**b**) obtained for $\theta_y = 5$. These curves are taken along the dashed lines (**a**) and (**b**) in Fig. 14 corresponding to $\theta_x = 2.7$ and $\theta_x = 6.5$, respectively. Full lines correspond to stable states, dashed lines correspond to unstable states, and dotted lines correspond to modulationally unstable states. Reproduced from [41]

finite width. This *front-locking mechanism* arises as a result of the complex balance between attractive and repulsive interactions occurring through the front oscillatory tails, with the stable structures being dissipative solitons.

The bifurcation diagram for these dark DSs, corresponding to the case with two distinct hysteresis loops shown in Fig. 15(a), is presented in Fig. 17. Similarly to the previous bifurcation diagrams, it was obtained through numerical continuation with a predictor–corrector algorithm that was initialized with a profile obtained by

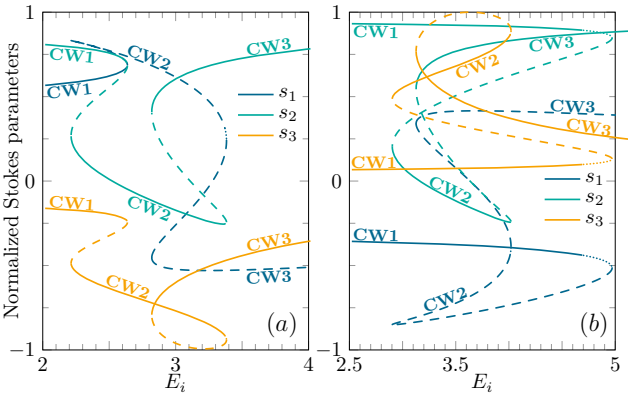

Fig. 16 (a) Stokes parameters of the CW solutions plotted in Fig. 15a and (b) Stokes parameters of the CW solutions plotted in Fig. 15b. The meaning of the dashed, dotted, and solid lines is the same as in Fig. 15. The parameters are the same as in Fig. 15. The injected light is linearly polarized, with $s_1 = s_3 = 0$ and s_2=1. Reproduced from [41]

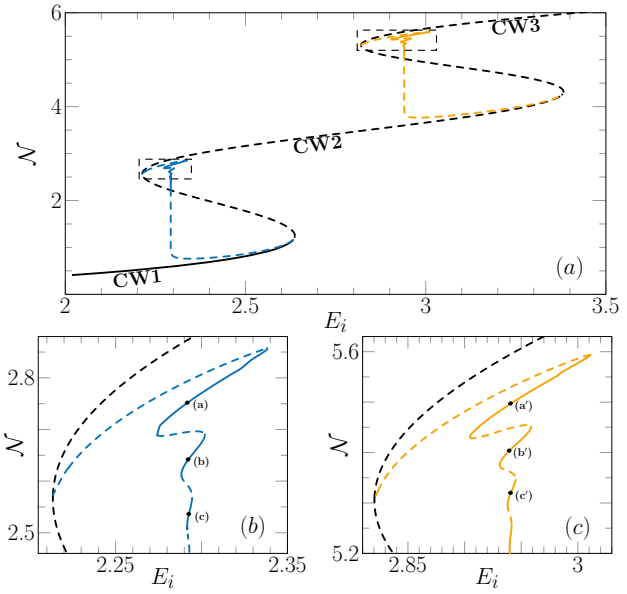

Fig. 17 (a) Bifurcation diagram showing the L2-norm $\mathcal{N}$ as a function of the injected field amplitude E_i. Stable (unstable) states are denoted by solid (dashed) lines. MI states are denoted by dotted lines. Parameters are $\theta_x = 2.7$ and $\theta_y = 5$. (b) Close-up on the snaking curves collapsing onto the Maxwell point of the left bistability. (c) Close-up on the snaking curves collapsing onto the Maxwell point of the right bistability. Reproduced from [41]

time-stepping numerical simulations with periodic boundary conditions. Two types of fronts can appear, connecting either CW3 with CW2, or CW2 with CW1. For each type of front, a type of DS can be stabilized, and the branches corresponding to each of these two types of dark DSs (light orange for the connection between CW3 with CW2 and dark blue for the connection between CW2 with CW1) present themselves again in the form of a collapsed snaking curve. They emerge from the saddle-node bifurcations corresponding to the appearance of CW3 and CW2 and connecting to the modulational instability bifurcation responsible for the loss of stability of, respectively, CW1 and CW2. We notice that the collapsed snakings exhibit more oscillations and that their amplitudes are larger compared to the previous section, which is explained by the fact that the hysteresis loops are wider than previous due to the higher value of the detuning parameters. The profiles of the Stokes parameters corresponding to the points (a)–(c) and (a′)–(c′) are depicted in Fig. 18 and show that again, each turning point leading to a new stable branch of dark DS corresponds to a new type of solution, with an additional bump at the bottom of the profile. As a dark DS corresponds to an excursion from a background corresponding to a CW solution into another CW solution for a short domain of the fast time τ, the Stokes parameters behave in the same way as the ones of the CW solutions. Since the CWs have very different polarization properties that are always elliptical, the DSs exhibit the same properties. DSs that belong to the same snaking curve share more or less the same polarization properties with slight variations as the shapes of the profiles differ. The differences between DSs that belong to different snaking curves are however more pronounced, as the two CWs involved are not the same in each case. This means that the background values, the peak powers as well as the Stokes parameters are all very different in this case. The spectra corresponding to the total intensity profiles of these solutions are again optical frequency combs, shown in Fig. 19. The frequency combs of the DSs share the same free spectral range regardless of their types, as they all share the same repetition rate.

The branch corresponding to modulationally unstable states is also shown in Fig. 20 to evidence that both collapsed snakings occur in a regime that is far enough from it, so that there can be no confusion between our front-locking-induced DSs and modulational instability-induced DSs.

The bifurcation diagram corresponding to the case with two overlapping hysteresis loops shown in Fig. 15b is presented in Fig. 21. This time, the two types of fronts connecting either CW3 with CW2, or CW2 with CW1 can appear for the same values of the system parameters, and so can the associated dark DSs. We obtain again a collapsed snaking bifurcation diagram for the branches corresponding to each of these two types of DSs (light orange for the connection between CW3 with CW2 and dark blue for the connection between CW2 with CW1), except that the two oscillating curves now overlap for a certain range of the injected field amplitude called C. As such, two types of dark DSs exist again, (a)–(c) connecting CW1 to CW2 and (a′)–(c′) connecting CW2 to CW3, shown in Fig. 22. The two types of DSs, similarly to the previous case, have very different peak powers, background values, and polarization properties. In the region C, the system can host dark DSs of the two types, (a)–(c) and (a′)–(c′). However, they cannot be hosted at the same time

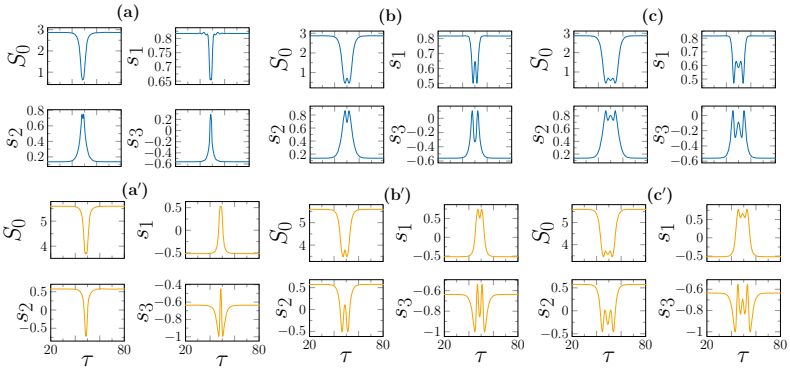

Fig. 18 Profiles of the Stokes parameters S_0, s_1, s_2, and s_3 as a function of the fast time τ for the stable DS solutions indicated in Fig. 17. The size of the system was taken as $L = 100$. Profiles (**a**)–(**c**) correspond to the region highlighted on the left, while (a′)–(c′) correspond to the region highlighted on the right. Injection amplitude values are E_i = (a) 2.2917, (b) 2.2922, (c) 2.2926 (a′) 2.9394, (b′) 2.9406, and (c′) 2.9406. Reproduced from [41]

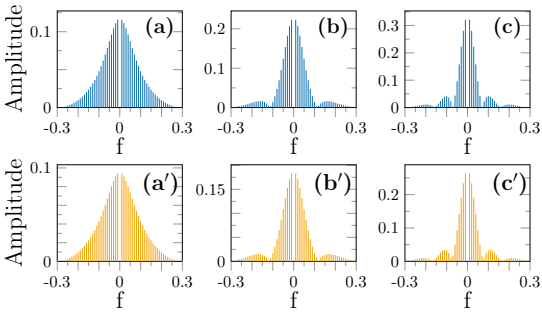

Fig. 19 Vector Kerr combs corresponding to Fourier transform of the stable DS solutions shown in Fig. 18. Reproduced from [41]

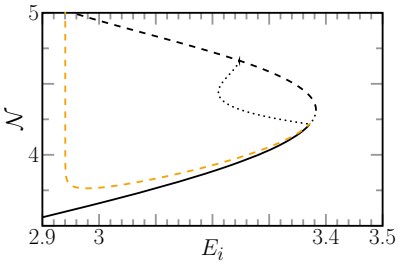

Fig. 20 Close-up showing the MI branch emerging from the end of the upper snaking curve from Fig. 17a. Reproduced from [41]

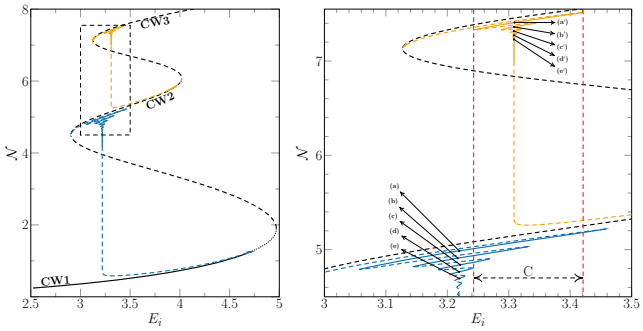

Fig. 21 Tristable heteroclinic snaking. Left panel: Bifurcation diagram showing the L2-norm $\mathcal{N}$ as a function of the injected field amplitude E_i. Stable (unstable) states are denoted by solid (dashed) lines. MI states are denoted with dotted lines. Parameters are $\theta_x = 6.5$ and $\theta_y = 4.5$. The size of the system was taken as $L = 200$. Right panel: Close-up on the snaking curves collapsing onto the Maxwell point of each respective bistability showing the coexistence region C. Reproduced from [41]

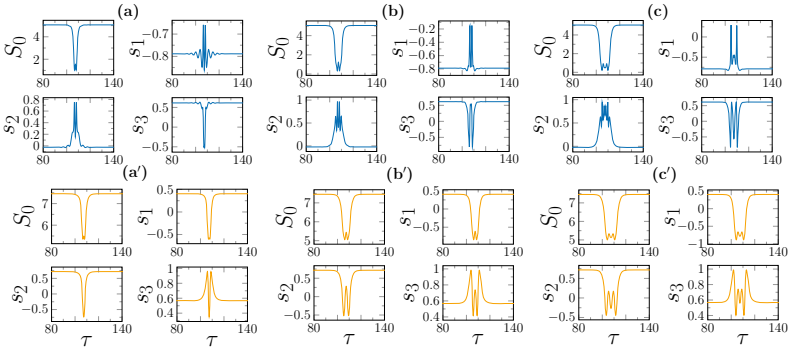

Fig. 22 Profiles of the Stokes parameters S_0, s_1, s_2, and s_3 as a function of the fast time τ for the stable solutions indicated in Fig. 21. Parameters are the same as in Fig. 21. Injection amplitude values are $E_i =$ (a) 3.2195, (b) 3.217, (c) 3.2209, (a′) 3.3094, (b′) 3.3087, and (c′) 3.3085. Reproduced from [41]

and in the same physical system as they require different background intensities. The combs corresponding to these profiles are drawn in Fig. 23. They share the same properties as the ones from Fig. 19, except for a different FSR that is only due to the fact we used a different cavity length in this case, for the sake of numerical convenience.

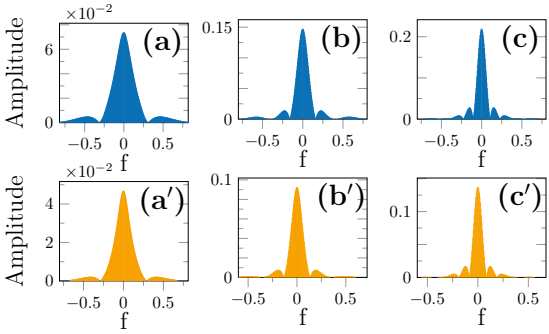

Fig. 23 Vector Kerr combs corresponding to the stable solutions shown in Fig. 22. Reproduced from [41]

6 Conclusions and Perspectives

We have investigated the formation of dissipative solitons in high-Q micro- and macro-resonators driven by a linearly polarized injected light. We have studied the influence of the polarization degrees of freedom in these optical resonators that are described by the vectorial Lugiato–Lefever equation. These additional degrees of freedom impact the homogeneous steady states solutions by creating a new critical second-order transition allowing for the generation of multistability. We have shown that there can be up to three coexisting stable solutions. Two operating regimes were considered: anomalous and normal dispersion.

In the anomalous dispersion regime, the linear stability analysis indicated that one or more homogeneous solutions suffer modulational instability. We have focused on the situation where two modulationally unstable homogeneous solutions coexist with one stable CW solution. Besides periodic solutions, an infinite number of DSs characterized by either a odd or even number of peaks coexist with the periodic and the CW solutions. The system can host two types of DSs, as the stable CW solution provides the continuous background needed to host them, and the system exhibits multistability. We have shown that their bifurcation diagram each follows an homoclinic snaking type of bifurcation. These two types of DSs exhibit different peak powers and polarization properties and can coexist in the same physical system.

In the normal dispersion regime, we first showed that for low values of the detuning, we obtain a bistable regime where DSs can be formed thanks to the interaction between switching waves, or front, connecting pairs of CW solutions. The bifurcation diagram of these DSs obeys collapsed heteroclinic snaking. Then, for higher values of the detuning, there can be up to the three coexisting CW solutions. The system can also host two types of DSs, each exhibiting a separate collapsed snaking. Again, the two types of DSs exhibit different peak powers and polarization properties. For the right values of the detuning parameters, these two collapsed snaking curves can have an overlapping domain of stability and the two types can coexist for the same values of the system parameters, however not in the same physical system.

These results bring new insights into the properties of dissipative structures in driven resonators when the polarization degrees of freedom are taken into account. In order to further complete the description, the influence of the group-velocity mismatch between the two polarization components should be considered. However neglected in the present study, this property can significantly impact the dynamics, as it leads to a drift of the DSs caused by a breaking of the $\tau \rightarrow -\tau$ symmetry.

Acknowledgements K.P. acknowledges support from the Fonds Wetenschappelijk Onderzoek-Vlaanderen FWO (G0E5819N) and the Methusalem Foundation. M.T. acknowledges financial support from the Fonds de la Recherche Scientifique FNRS under Grant CDR no. 35333527 "Semiconductor optical comb generator". A part of this work is supported by the "Laboratoire Associé International" University of Lille—ULB on "Self-organization of light and extreme events" (LAI-ALLURE).

References

1. I. Prigogine, R. Lefever, Symmetry breaking instabilities in dissipative systems. ii. J. Chem. Phys. **48**(4), 1695–1700 (1968)
2. P. Glansdorff, I. Prigogine, *Thermodynamic Theory of Structure, Stability and Fluctuations* (Willey, 1971)
3. V. Castets, E. Dulos, J. Boissonade, P. De Kepper, Experimental evidence of a sustained standing turing-type nonequilibrium chemical pattern. Phys. Rev. Lett. **64**(24), 2953–2957 (1990)
4. Q. Ouyang, H.L. Swinney, Transition from a uniform state to hexagonal and striped turing patterns. Nature **352**, 610–612 (1991)
5. J.D. Murray, *Mathematical Biology I (An Introduction* (Springer, Berlin, 2001)
6. R. Lefever, O. Lejeune, On the origin of tiger bush. Bull. Math. Biol. **59**(2), 263–294 (1997)
7. M. Rietkerk, S.C. Dekker, P.C. De Ruiter, J. van de Koppel, Self-organized patchiness and catastrophic shifts in ecosystems. Science **305**(5692), 1926–1929 (2004)
8. M. Tlidi, R. Lefever, A. Vladimirov, On vegetation clustering, localized bare soil spots and fairy circles, in *Dissipative Solitons: From Optics to Biology and Medicine* (Springer, 2008), pp. 1–22
9. M. Tlidi, K. Staliunas, K. Panajotov, A.G. Vladimirov, M.G. Clerc, Localized structures in dissipative media: from optics to plant ecology (2014)
10. L.A. Lugiato, R. Lefever, Spatial dissipative structures in passive optical systems. Phys. Rev. Lett. **58**(21), 2209 (1987)
11. A.J. Scroggie, W.J. Firth, G.S. McDonald, M. Tlidi, R. Lefever, L.A. Lugiato, Pattern formation in a passive kerr cavity. Chaos, Solitons & Fractals **4**(8–9), 1323–1354 (1994)
12. M. Tlidi, K. Panajotov, Cavity solitons: dissipative structures in nonlinear photonics. Rom. Rep. Phys **70**, 406 (2018)
13. G. Kozyreff, M. Tlidi, Optical patterns with different wavelengths. Phys. Rev. E **69**, 066202 (2004). (Jun)
14. M. Tlidi, P. Mandel, R. Lefever, Localized structures and localized patterns in optical bistability. Phys. Rev. Lett. **73**(5), 640 (1994)
15. W. van Saarloos, P.C. Hohenberg, Fronts, pulses, sources and sinks in generalized complex Ginzburg-Landau equations. Phys. D: Nonlinear Phenom. **56**(4), 303–367 (1992)
16. N.N. Rosanov, I transverse patterns in wide-aperture nonlinear optical systems. Prog. Opt. **35**, 1–60 (1996)
17. U. Bortolozzo, S. Residori, Storage of localized structure matrices in nematic liquid crystals. Phys. Rev. Lett. **96**(3), 037801 (2006)

18. A. Jacobo, D. Gomila, M.A. Matías, P. Colet, Logical operations with localized structures. New J. Phys. **14**(1), 13040 (2012)
19. F. Pedaci, G. Tissoni, S. Barland, M. Giudici, J. Tredicce, Mapping local defects of extended media using localized structures. Appl. Phys. Lett. **93**(11), 111104–111104-3 (2008)
20. C. Mou, S.V. Sergeyev, A.G. Rozhin, S.K. Turitsyn, Bound state vector solitons with locked and precessing states of polarization. Opt. Express **21**(22), 26868–26875 (2013)
21. X. Hu, J. Guo, G.D. Shao, Y.F. Song, L.M. Zhao, L. Li, D.Y. Tang, Dissipative dark-bright vector solitons in fiber lasers. Phys. Rev. A **101**, 063807 (2013)
22. V. E. Lobanov, A. E. Shitikov, R. R. Galiev, K. N. Min'kov, O. V. Borovkova, N. M. Kondratiev, Generation of vector flat-top solitons and hybrid bright-flat-top soliton complexes in optical microresonators via modulated pump. Phys. Rev. A **104**, 063511 (2021). (Dec)
23. S.V. Sergeyev, C. Mou, E.G. Turitsyna, A. Rozhin, S.K. Turitsyn, K. Blow, Spiral attractor created by vector solitons. Light.: Sci. & Appl. **3**(1), e131 (2014)
24. C. Mou, S. Sergeyev, A. Rozhin, S. Turistyn, All-fiber polarization locked vector soliton laser using carbon nanotubes. Opt. Lett. **36**(19), 3831–3833 (2011)
25. S.T. Cundiff, B.C. Collings, N.N. Akhmediev, J.M. Soto-Crespo, K. Bergman, W.H. Knox, Observation of polarization-locked vector solitons in an optical fiber. Phys. Rev. Lett. **82**(20), 3988–3991 (1999)
26. V.J. Sánchez-Morcillo, I. Pérez-Arjona, G.J. de Valcárcel F. Silva, E. Roldán, Vectorial kerr-cavity solitons. Opt. Lett. **25**(13), 957–959 (2000)
27. S.V. Sergeyev, C. Mou, A. Rozhin, S.K. Turitsyn, Vector solitons with locked and precessing states of polarization. Opt. Express **20**(24), 27434–27440 (2012)
28. V. Tsatourian, S.V. Sergeyev, C. Mou, A. Rozhin, V. Mikhailov, B. Rabin, P. S. Westbrook, S.K. Turitsyn, Polarisation dynamics of vector soliton molecules in mode locked fibre laser. Sci. Rep. **3**, 3154 (2013)
29. F. Leo, S. Coen, P. Kockaert, S.-P. Gorza, P. Emplit, M. Haelterman, Temporal cavity solitons in one-dimensional kerr media as bits in an all-optical buffer. Nat. Photonics **4**(7), 471–476 (2010)
30. A.B. Matsko, A.A. Savchenkov, W. Liang, V.S. Ilchenko, D. Seidel, L. Maleki, Mode-locked kerr frequency combs. Opt. Lett. **36**(15), 2845–2847 (2011)
31. L.A. Lugiato, F. Prati, M.L. Gorodetsky, T.J. Kippenberg, From the Lugiato–Lefever equation to microresonator-based soliton kerr frequency combs. Philos. Trans. R. Soc. A: Math., Phys. Eng. Sci. **376**(2135), 20180113 (2018)
32. P.J. Delfyett, S. Gee, M-T. Choi, H. Izadpanah, W. Lee, S. Ozharar, F. Quinlan, T. Yilmaz, Optical frequency combs from semiconductor lasers and applications in ultrawideband signal processing and communications. J. Lightwave Technol. **24**(7), 2701 (2006). (Jul)
33. Y.K. Chembo, Kerr optical frequency combs: theory, applications and perspectives. Nanophotonics **5**(2), 214–230 (2016)
34. T.J. Kippenberg, A.L. Gaeta, M. Lipson, M.L. Gorodetsky, Dissipative kerr solitons in optical microresonators. Science **361**(6402), eaan8083 (2018)
35. T. Fortier, E. Baumann, 20 years of developments in optical frequency comb technology and applications. Commun. Phys. **2**(1) (2019)
36. M. Lipson, J.S. Levy, A. Gondarenko, M.A. Foster, A.C. Turner-Foster, A.L. Gaeta, Cmos-compatible multiple-wavelength oscillator for on-chip optical interconnects. Nat. Photonics **4**(1), 37–40 (2010)
37. P. Del'Haye, T. Herr, E. Gavartin, M.L. Gorodetsky, R. Holzwarth, T.J. Kippenberg, Octave spanning tunable frequency comb from a microresonator. Phys. Rev. Lett. **107**, 063901 (2011). (Aug)
38. A.A. Savchenkov, A.B. Matsko, W. Liang, V.S. Ilchenko, D. Seidel, L. Maleki, Kerr combs with selectable central frequency. Nat. Photonics **5**(5), 293–296 (2011)
39. R.A. Chipman, W.-S.T. Lam, G. Young. *Polarized Light and Optical Systems* (CRC Press, 2018)
40. G.P. Agrawal, *Nonlinear Fiber Optics*, 6th Edn. (Academic Press, 2019)

41. Kostet, Y. Soupart, K. Panajotov, M. Tlidi, Coexistence of dark vector soliton Kerr combs in normal dispersion resonators. Phys. Rev. A **104**, 053530 (2021)
42. M. Haelterman, S. Trillo, S. Wabnitz, Polarization multistability and instability in a nonlinear dispersive ring cavity. J. Opt. Soc. Am. B **11**, 446–456 (1994)
43. T. Hansson, M. Bernard, S. Wabnitz, Modulational instability of nonlinear polarization mode coupling in microresonators. J. Opt. Soc. Am. B **35**, 835–841 (2018)
44. A.U. Nielsen, B. Garbin, S. Coen, S.G. Murdoch, M. Erkintalo, Coexistence and interactions between nonlinear states with different polarizations in a monochromatically driven passive kerr resonator. Phys. Rev. Lett. **123**, 013902 (2019)
45. S. Coen, M. Tlidi, Ph. Emplit, and M. Haelterman, Convection versus Dispersion in Optical Bistability. Phys. Rev. Lett. **83**, 2328 (1999)
46. E. Averlant, M. Tlidi, K. Panajotov, L. Weicker, Coexistence of cavity solitons with different polarization states and different power peaks in all-fiber resonators. Opt. Lett. **42**, 2750–2753 (2017)
47. J. Burke, E. Knobloch, Homoclinic snaking: structure and stability. Chaos: Interdiscip. J. Nonlinear Sci. **17**(3), 037102 (2007)
48. P. Parra-Rivas, E. Knobloch, D. Gomila, L. Gelens, Dark solitons in the Lugiato-Lefever equation with normal dispersion. Phys. Rev. A **93**, 063839 (2016). (Jun)
49. B. Kostet, S. S. Gopalakrishnan, E. Averlant, Y. Soupart, K. Panajotov, and M. Tlidi, Vectorial dark dissipative solitons in Kerr resonators. OSA Continuum **4**, 1564–1570 (2021)
50. P. Coullet, L. Gil, D. Repaux, Defects and subcritical bifurcations. Phys. Rev. Lett. **62**(25), 2957 (1989)
51. J. Knobloch, T. Wagenknecht, Homoclinic snaking near a heteroclinic cycle in reversible systems. Phys. D: Nonlinear Phenom. **206**(1–2), 82–93 (2005)
52. Y.-P. Ma, J. Burke, E. Knobloch, Defect-mediated snaking: a new growth mechanism for localized structures. Phys. D: Nonlinear Phenom. **239**(19), 1867–1883 (2010)
53. A. Dhooge, W. Govaerts, Yu.A. Kuznetsov, Matcont: a matlab package for numerical bifurcation analysis of odes. ACM Trans. Math. Softw. (TOMS) **29**(2), 141–164 (2003)